

ARTICLE OPEN

Unveiling the origin of *n*-type doping of natural MoS₂: carbon

Youngsin Park^{1,7}, Nannan Li^{2,7}, Daesung Jung^{3,7}, Laishram Tomba Singh^{4,7}, Jaeyoon Baik⁴, Eunsook Lee⁴, Dongseok Oh⁴, Young Dok Kim², Jin Yong Lee², Jeongseok Woo⁵, Seungmin Park⁵, Hanchul Kim⁶, Geunseop Lee⁵, Geunsiik Lee¹ and Chan-Cuk Hwang⁴

MoS₂ has attracted intense interest in many applications. Natural MoS₂ and field-effect transistors made of it generally exhibit *n*-type characteristics, but its origin is unknown. Herein, we show that C is the origin of the universal *n*-type doping of natural MoS₂. Photoemission spectroscopies reveal that while many MoS₂ samples with C detected are *n*-type, some without C exhibit *p*-type characteristics. The C-free, *p*-type MoS₂ changes to *n*-type over time with the concurrent appearance of C that is out-diffused from bulk, indicating that C induces the *n*-type doping. The C-origin is verified by C-deposition and supported by theoretical calculations. This carbon appears as nanometer-scale defects frequently observed in scanning tunneling microscopy. In addition, we propose, based on the calculations, that S vacancies are responsible for the *p*-type characteristics, which contrasts with the widespread belief. This work provides new perspectives on MoS₂ doping and presents a new direction for fabricating reliable MoS₂ devices.

npj 2D Materials and Applications (2023)7:60; <https://doi.org/10.1038/s41699-023-00424-x>

INTRODUCTION

As layered two-dimensional (2D) materials, transition metal dichalcogenides (TMDs) have attracted intense interest owing to their unique properties that are potentially advantageous for applications in wide areas^{1–3}. Molybdenum disulfide (MoS₂) is an archetypal TMD material with potential in electronic^{4–6}, optoelectronic^{7,8}, photovoltaic^{9,10}, catalytic^{11,12}, and sensing¹³ applications. Since the successful realization of field-effect transistor (FET) devices using a single or few MoS₂ layer channel⁴, considerable research has focused on high-performance and novel electronic and optoelectronic devices using various 2D materials^{14–16}. The device performance is affected by intrinsic factors (quality of the materials with defects, including structural imperfections and unintentional impurities) and extrinsic factors (doping from substrates and surface adsorbates, metal-semiconductor junction causing a Schottky barrier). Extensive efforts have been devoted to enhancing the device's performance, focusing mainly on extrinsic factors. Notable progress has been made, for example, through encapsulation¹⁷, dielectric interface engineering¹⁸, and reduction of the Schottky barrier height¹⁹. It is also important to improve the inherent properties of MoS₂, which are determined by intrinsic factors. As a first step, it is essential to clarify the carrier type and work function (WF) and identify the defects present in natural or grown MoS₂. Such basic knowledge can be exploited to fabricate high-performance devices.

Most MoS₂ FETs exhibit *n*-type transport behavior^{4–7,13,20–23} while ambipolar transport was also reported in some studies^{24,25}. The band structure of MoS₂ measured using angle-resolved photoemission spectroscopy (ARPES) showed unanimously that the valence band is located well below the Fermi level (E_F) (>1 eV)^{26–30}. These have led to the speculation that natural MoS₂ without intentional doping is an *n*-type semiconductor. The intrinsic *n*-type MoS₂ was often attributed to S vacancies, which were believed to be the most abundant and probable defects in MoS₂ owing to its small formation energy^{31–34}. On the other hand,

the role of S vacancies as electron donors was not supported by most theoretical studies^{35–38}. Other impurities, such as Cl or Br⁷, Re³⁶, and H³⁸, have been suggested as alternative causes of *n*-type doping. Scanning tunneling microscopy (STM) studies have shown that S vacancies and other defects are present near the MoS₂ surfaces^{33,39–41}. These near-surface defects were postulated to act as unintended dopants, but their nature has not been identified. Therefore, identifying these intrinsic defects in MoS₂ remains elusive, and a consistent understanding of the origin of the predominantly observed *n*-type properties is lacking.

Here, we present evidence that *n*-type doping of MoS₂ is provided by carbon (C) atoms through studies combining photoemission spectroscopy (PES), STM, and density-functional theory (DFT) calculations. ARPES data have shown that the E_F of the newly exfoliated MoS₂ is located near the valence band maximum (VBM) when C atoms are not detected. As the amount of C increases over time, the E_F gradually moves away from the VBM with a concurrent decrease in the WF, indicating that the C impurity induces a change in doping from *p*- to *n*-type. STM showed that the nanometer-scale defects commonly observed on MoS₂ surfaces increased in number over time, indicating their correlation with C atoms. All these experimental observations correlated to the increasing amounts of C were confirmed by intentionally depositing C atoms on the MoS₂ surface. DFT calculations corroborated the C-induced doping change from *p*- to *n*-type and the WF variation. Theoretical results also suggest that the initial *p*-type doping observed in the absence of carbon is attributed to S vacancies at the surface.

RESULT AND DISCUSSION

Angle-resolved photoemission spectroscopy

Although MoS₂ is one of the representative 2D layered materials, it has a sizable band dispersion (as much as 0.5 eV) in the direction

¹Department of Chemistry, College of Natural Science, Ulsan National Institute of Science and Technology, Ulsan 44919, Korea. ²Department of Chemistry, Sungkyunkwan University, Suwon 16419, Korea. ³Convergence Research Center for Energy and Environmental Science, Sungkyunkwan University, Suwon 16419, Korea. ⁴Pohang Accelerator Laboratory, Pohang University of Science and Technology, Pohang 37673, Korea. ⁵Department of Physics, Inha University, Incheon 22212, Korea. ⁶Department of Applied Physics, Sookmyung Women's University, Seoul 04310, Korea. ⁷These authors contributed equally: Youngsin Park, Nannan Li, Daesung Jung, Laishram Tomba Singh.

✉email: ysinpark@unist.ac.kr; glee@inha.ac.kr; gslee@unist.ac.kr; cchwang@postech.ac.kr

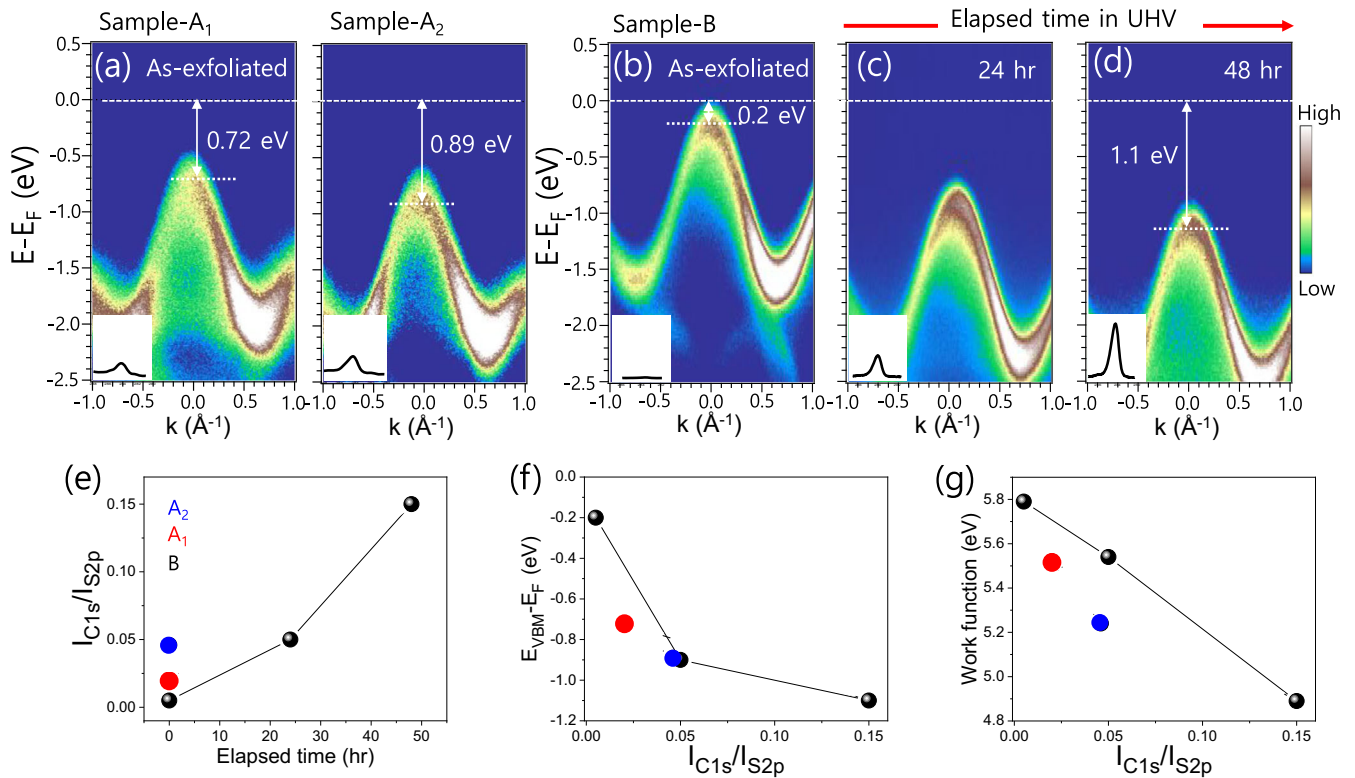


Fig. 1 ARPES and PES spectra with different samples. **a** ARPES data showing electronic band structures for different MoS₂ samples. Samples-A₁ and A₂ with noticeable amounts of carbon were obtained immediately after exfoliation in the UHV of 1.3×10^{-10} Torr. **b** Another sample-B with a small amount of carbon immediately after exfoliation under UHV, **c** after 24 h, and **d** after 48 h. ARPES data were taken at the photon energy of 56 eV along the Γ -K symmetry direction of the surface Brillouin zone. The color scales in the figures are the same. Insets show C 1s PES spectra corresponding to the ARPES data. **e** Relative peak intensity of C 1s to S 2p (I_{C1s}/I_{S2p}) for samples-A₁, A₂, and B with time. **f** VBM of MoS₂ as a function of I_{C1s}/I_{S2p} . **g** WF of MoS₂ as a function of I_{C1s}/I_{S2p} .

perpendicular to the layers due to interlayer coupling⁴². Therefore, it is crucial to use the appropriate photon energy (56 eV) to determine the VBM accurately when measuring the in-plane band structure (Supplementary Fig. 1). Figure 1a shows experimental band structures measured immediately after exfoliation in ultra-high vacuum (UHV) for representative MoS₂ samples (samples-A₁ and A₂). Many of the investigated samples showed similar data, and overall features (including the VBM at approximately -0.7 to -0.9 eV relative to E_F) are in good agreement with previous results^{26–30}. For some freshly exfoliated samples [sample-B in Fig. 1b], ARPES data show rigid energy shifts with a similar band structure to those of Fig. 1a. The exact VBM was determined after taking the constant energy map (Supplementary Fig. 2). The VBM located at -0.2 eV is very close to the E_F , which is very unusual. Considering the bulk band gap of 1.2–1.3 eV, samples-A₁ and A₂ and sample-B are *n*- and *p*-type semiconductors, respectively, exhibiting the variability of MoS₂ in doping. Sample-B, being initially *p*-type, showed a shift of the E_F upward from the VBM with time [Fig. 1b–d]. The VBM shifted down by ~ 0.7 eV after 24 h of aging under UHV without any treatment. After 48 h of aging, the VBM was lowered further, reaching ~ -1.1 eV. This indicates that a change in the doping type of the MoS₂ toward *n*-type occurs over time. In order to prove the reproducibility, we tested a number of pristine-MoS₂ samples. About 20–30% of them showed *p*-type properties, and the others presented *n*-type properties depending on the carbon amount. In addition to the change in the VBM, the measured WF also changed over time. The WF of sample-B (5.8 eV) was initially larger than those of the freshly exfoliated samples-A₁ and A₂ (WF = 5.2–5.5 eV). However, the WF of sample-B decreased with time and reached 4.9 eV after 48 h, similar to the typical value

for the *n*-type MoS₂. High-resolution core-level PES was used to explain the differences in VBM and WF between different MoS₂ samples [insets of Fig. 1a–d and Supplementary Fig. 3]. When the carbon-free sample was kept in the UHV chamber for a long time, the C 1s peak began to appear and grew slowly over time [insets of Fig. 1c, d, and Supplementary Fig. 3b]. We also investigated the possible adsorption of other adsorbates, such as O₂ and H₂O. Wide spectra taken over time with a photon energy of 630 eV confirm that no other adsorbates are detected except for C (Supplementary Fig. 4).

Figure 1e plots the C_{1s}/S_{2p} peak intensity ratio (I_{C1s}/I_{S2p}) as a function of time for sample-B (data for the as-exfoliated samples-A₁, A₂ are also shown). Figure 1f, g shows the observed VBM and the WF as functions of I_{C1s}/I_{S2p} , respectively. The strong dependence on the carbon content is evident, suggesting that the carbon is responsible for the time-dependent changes in the electronic properties. The correlation of the time-dependent changes in the VBM and the WF to the measured carbon content was well reproduced.

Carbon was deposited directly onto the MoS₂ to clarify the origin of the time-dependent changes shown in Fig. 1. Figure 2a shows the band structure of a MoS₂ containing trace amounts of carbon, where the VBM is very close to the E_F . When carbon was deposited for 5, 10, 15, and 20-min [Fig. 2b–e], the VBM moved down relative to E_F . Finally, the VBM was lowered to -1.18 eV after 20-min deposition. The I_{C1s}/I_{S2p} in Fig. 2f shows that the amount of carbon increased with deposition time. Both the VBM [Fig. 2g] and WF [Fig. 2h] decreased almost linearly with increasing I_{C1s}/I_{S2p} . The results were entirely consistent with the observed aging-induced changes. This shows that carbon is the origin of the changes in the VBM and WF.

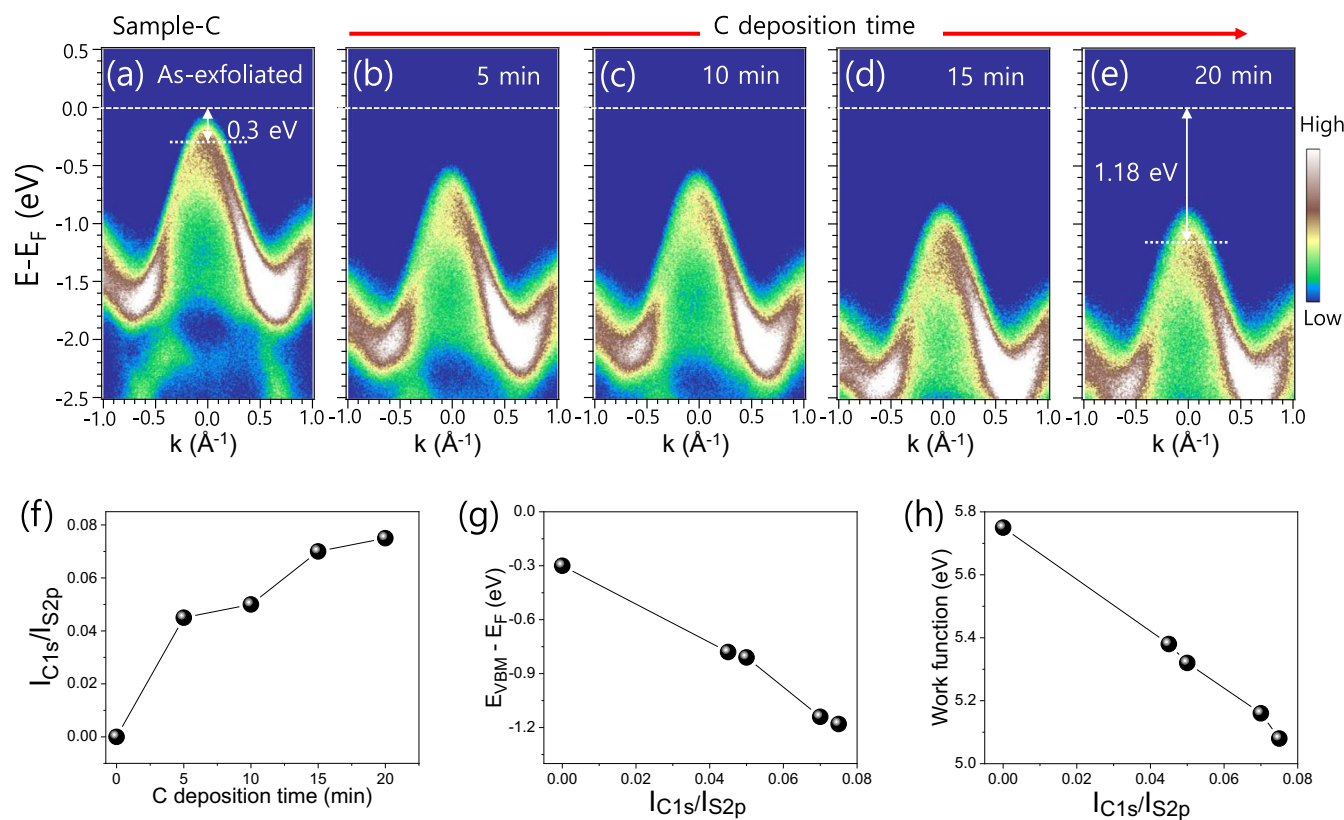


Fig. 2 ARPES with increasing carbon amounts. **a–e** Evolution of electronic band structures of the as-exfoliated MoS₂ (sample-C) with increasing carbon deposition. **f** I_{C1s}/I_{S2p} as a function of the carbon deposition time. **g** VBM of the MoS₂ as a function of I_{C1s}/I_{S2p} . **h** WF of the MoS₂ as a function of I_{C1s}/I_{S2p} .

Scanning tunneling microscopy

Figure 3 shows STM images of MoS₂. Several point defects are shown in the freshly exfoliated surface [Fig. 3a]. These defects are a few nanometers in size and are distinct from S vacancies that appear on the atomic scale (Supplementary Fig. 5). Two types of nanometer-scale defects could be distinguished at negative sample bias (i.e., in filled-state image): one appearing as bright elevations and the other as dark depressions [inset of Fig. 3b]. Both defects appear dark and are almost indistinguishable at positive sample bias (not shown). These nanometer-scale defects increased in number over time, as shown in a representative image of the MoS₂ surface obtained after 10 days [Fig. 3b]. No other new defects were observed. Previous STM studies also reported observations of these nanometer-scale defects commonly present on MoS₂ surfaces^{32–34,39–41}. In some studies, these defects have been attributed to S-vacancies^{32,33}. On the other hand, S vacancies were imaged independently as atomic-scale features^{40,43} (Supplementary Fig. 6). Thus, the observed nanometer-scale defects cannot be S vacancies, and their origin is still unknown. Considering that the amount of C in the PES data increased with aging, the nanometer-scale defects in STM images could be attributed to C-related features. Therefore, the MoS₂ surface was also investigated after C atoms were deposited to test the C-related origin of the nanometer-scale defects observed in STM images. Figure 3c–e shows the change in the MoS₂ surface with increasing C deposition (deposition time is changed while the other deposition parameters are fixed). The C-deposited surface exhibited the same nanometer-scale defects as those observed on the as-exfoliated and the aged surfaces [inset of Fig. 3d]. No other new defect features were observed. The number of “bright” (B) and “dark” (D) defect features in the filled-state image increased with increasing C deposition time [Fig. 3f],

suggesting that both defects are related to C atoms. The consistency between aging and C-deposited samples clearly shows that nanometer-scale defects commonly observed on MoS₂ surfaces originate from C atoms.

In many studies, the almost universal *n*-type characteristics of the MoS₂ materials and transistor devices based on them were attributed to S vacancies. This widely held belief originates from the consideration that the intrinsic S vacancies are prevalent on the surface because of their small formation energy. With the same reasoning, the nanometer-scale defects observed frequently in STM images were often interpreted as S vacancies with one or a few missing S atoms^{32–34}. On the other hand, the present study showed that the nanometer-scale defects are clearly distinguished from S vacancies, which is consistent with a recent study⁴⁰. Indeed, those defects are closely related to C impurities.

Density-functional theory calculations

DFT calculations were performed to investigate the origin of the carbon-induced *n*-type doping behavior of MoS₂. In addition to the native S vacancy (V_S), atomic C impurities at the surface were considered, such as the S-substituting C defect (C_S) and the interstitial C defects. Figure 4a shows the local atomic structures around V_S , C_S , and two interstitial C defects (C_{int} and C'_{int}), as well as the pristine (i.e., defect-free) case. C_{int} resembles a CS dimer substituting an S atom, whereas C'_{int} involves a C atom at the hollow site above Mo. C_{int} was found to be the lowest energy structure among all the interstitial defects we considered, which include metastable structures with C residing within the van der Waals (vdW) gap (Supplementary Fig. 6). Figure 4b shows the band structures, where all the energy levels are relative to VBM. The pristine band structure shows an indirect band gap, and the E_F is set to the midgap (0.62 eV above VBM). For V_S , the nearly flat

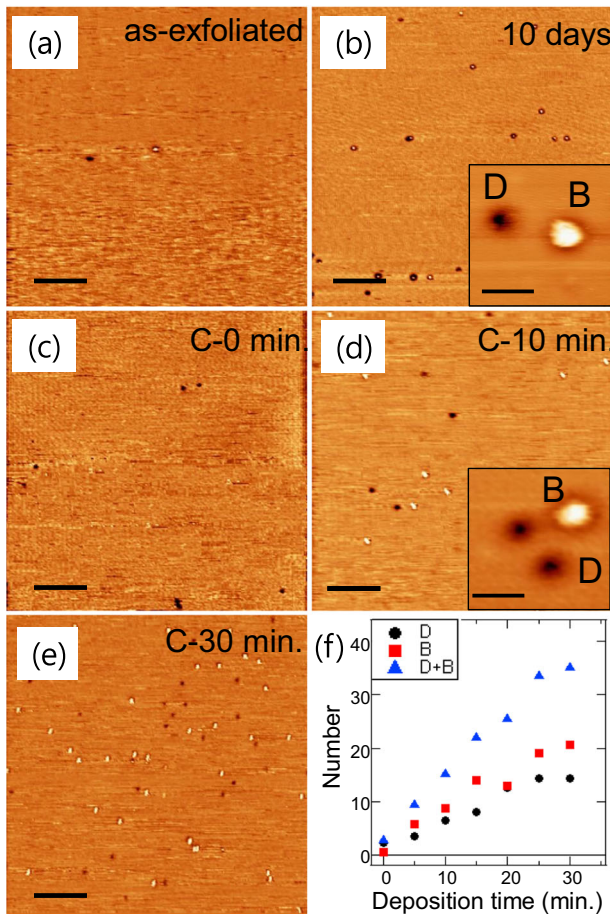


Fig. 3 STM images. STM images of aging effect: as-exfoliated (a) and after 10 days of aging (b). Effect of C deposition with varying deposition time: 0 min (as-exfoliated) (c), 10 min (d), and 30 min (e). All scale bars are 40 nm in (a–e), 4 nm for insets of (b) and (d). **f** The number of defects imaged per frame as a function of the C deposition time. Images were obtained with $V_s = -1.0$ V and $I_t = 0.3$ nA. Insets in (b) and (d) are zoomed-in images ($V_s = -1.0$ V and $I_t = 0.1$ nA) showing the bright (B) and dark (D) defects. The defects that appeared with aging and after C deposition are the same.

bands (blue symbols) caused by Mo dangling bonds appeared at -0.39 eV (occupied) and 0.81 eV (unoccupied). This shifts the E_F (0.40 eV) closer to VBM compared with the pristine case, which is consistent with the literature^{35,36}. Therefore, the MoS_2 surface with V_s exhibits p -type characteristics.

In the band structure of a surface with C_s , the dangling bond states of Mo disappear, and an unoccupied C-induced gap state (red symbols) appears at approximately 0.70 eV. Therefore, the E_F is lowered to 0.31 eV, exhibiting p -type behavior similar to V_s . For the two interstitial C defects C_{int} (C'_{int}), two C-induced bands appeared: one occupied at ~ 0.4 (0.6) eV and the other unoccupied at ~ 1.2 (1.1) eV. The resulting E_F at 0.80 (0.81) eV was raised toward CBM by about 0.18 (0.19) eV, compared with the pristine case. This suggests that both interstitial C defects C_{int} and C'_{int} exhibit n -type behavior, which is different from the p -type behavior of V_s and C_s defects.

The WFs were calculated for the pristine and the defected MoS_2 surfaces. The WF increased for V_s (5.28 eV) and C_s (5.37 eV) but decreased for C_{int} (4.88 eV) and C'_{int} (4.87 eV) compared to the pristine surface (5.06 eV). The changes in the E_F and the WF due to C_{int} and C'_{int} are consistent with the C-induced changes observed in the ARPES experiments. Therefore, the p -type observed for

freshly exfoliated MoS_2 is attributed to V_s and possibly to C_s , and the carbon defects causing the n -type are ascribed to interstitial C. Two interstitial C (C_{int} and C'_{int}) configurations are matched with the two experimental nanometer-scale defect types (B and D). However, we are not able to match which of the experimental defects corresponds to which theoretical interstitial C configurations due to the limited STM images and the difficulties of simulating such large-size defects.

Based on the theoretical calculations, we propose that S vacancies or S-substituting C atoms induce p -type behavior, accounting for the observed E_F close to the VBM [Fig. 1b]. This proposition contradicts the prevailing belief that S vacancies are responsible for n -type behavior^{31–34}. Whereas the supporting evidence showing that S vacancies induce p -type can also be found in previous studies. Several PES studies have reported the change in MoS_2 from n - to p -type upon thermal annealing^{44,45} and ion irradiation^{46,47}. Because S vacancies are expected to be generated in those processes, the n - to p -type change was correlated with S vacancies. Previous STM and scanning tunneling spectroscopy (STS) data obtained near atomic-scale defects, considered neutral S-vacancy defects, showed the E_F close to the VBM, which is indicative of p -type. All these previous studies support the proposition that S vacancies (S-substituting C atoms) induce p -type properties rather than n -type properties. The change from p - to n -type is due to the near-surface C impurities (interstitial C), which increase in amount over time.

A previous study has reported that as-exfoliated MoS_2 surfaces exhibit almost intrinsic properties, whereas surface electron accumulation (SEA) occurs upon prolonged exposure to air⁴⁸. STS and ARPES data indicated a shift in the E_F toward the conduction band in the aged samples, which is consistent with SEA. The authors attributed the SEA to the formation of S vacancies caused by a slow desulfurization process based on the unsubstantiated correlation between the prevailing n -type behavior and the expected predominance of S vacancies. On the other hand, our experimental observations and theoretical calculations clearly show that the change from p - to n -type is due to near-surface C impurities. Evidently, the C impurities (interstitial C) are the origin of the universally observed n -type properties of the MoS_2 . Note that there was an older publication reporting a decrease in electron affinity and ionization potential with surface contamination by C⁴⁹, which is consistent with the C origin of n -type MoS_2 demonstrated in our study.

The remaining question to be answered is where the C impurity atoms originate. The C impurity was recently reported for another TMD, WS_2 monolayer synthesized by chemical vapor deposition (CVD)^{50,51}. In those studies, CH substituting for S atoms (CH_3) was proposed as the most stable C-related point defect on monolayer WS_2 in the plasma-enhanced CVD environment with methane gas. The possibility of the external origin of the C-related impurities on our MoS_2 from residual C-containing molecules in UHV was tested by dosing C_2H_2 and CO gases. Despite the significant amounts of dosing, C_2H_2 resulted in no changes in the band structure, whereas CO induced a slight downward shift of the VBM. However, the change was too small to account for the temporal changes (Supplementary Fig. 7). Note that the CH_3 defects on monolayer WS_2 show similar nanometer-scale STM contrast to the B defects on MoS_2 ⁵¹. CH incorporation is a possible high-temperature process in hydrocarbon-containing environments, but since our experiments were not carried out in such environments, we rule out the possibility of the CH_3 as C-related defects on MoS_2 .

Our DFT calculations show that carbon atoms favor near-surface regions (Supplementary Fig. 8), so there exists a net thermodynamic driving force for outward C diffusion. The inner C atoms will diffuse mainly along paths whose energy barriers are relatively lower than others. We speculate the diffusion path consisting of (1) horizontal hoppings from one C_{int} site to neighboring C_{int} sites

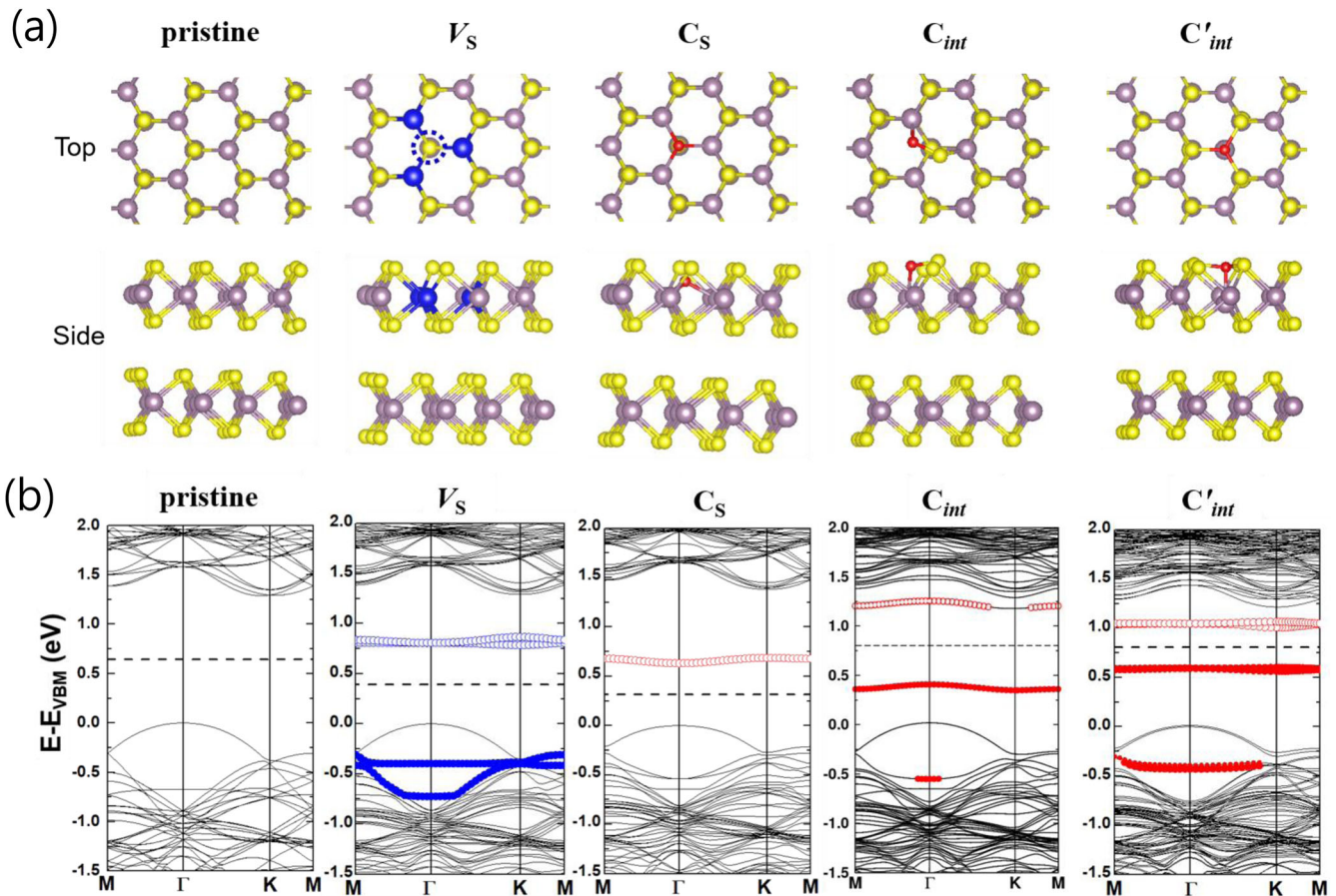


Fig. 4 DFT calculations. **a** Top and side views of pristine MoS₂, defective ones with S vacancy (V_S), S-substituting C defect (C_S), and two interstitial C defects (C_{int} and C'_{int}). Atomic defects are located at the outermost atomic layer. The bright purple, yellow, and red balls denote the Mo, S, and C atoms, respectively, while the three blue balls are Mo atoms adjacent to V_S (indicated by the dashed circle). **b** Band structures of pristine and defective MoS₂ bilayers using a 4×4 supercell. The horizontal dashed line indicates the E_F set to be the center of the energy gap. The blue and red circles denote the major contributions of Mo atoms with the dangling bonds and C atoms, respectively. The solid and open circles indicate the occupied and unoccupied states, respectively. All the energy levels are aligned relative to the VBM for easy recognition of the E_F shift.

via C'_{int} , (2) vertical hoppings across vdW gaps, and (3) penetrations through atomic (MoS₂) layers. Our calculations of hopping barriers suggest that the vertical hopping across the vdW gap is much slower than the horizontal hopping (Supplementary Fig. 9). While C impurities hardly go through complete MoS₂ layers, they will be able to cross each MoS₂ layer through sufficiently large voids. Since chemically active sites around voids are more likely to be passivated, the associated penetration of C atoms is expected to be relatively easy. Therefore, we estimate the outward diffusion length to be of the order of sub-micrometer per one day at room temperature (RT) (see Supplementary Note 8). It matches reasonably well with the experimental time scale to observe an increased amount of C atoms.

The C atoms can exist in different configurations, C_{int} (or C'_{int}) and C_S , when the MoS₂ sample contains V_S defects. The calculated formation energies of considered defects indicate that a C_S defect is more stable by 4.5 eV than coexisting single defects of V_S and C_{int} . This implies that C impurity atoms tend to form C_S defects by occupying the existing S vacancies. As discussed above, C impurity atoms would diffuse outward over time after exfoliation, whose form is likely to be C_{int} and change to C_S by sitting down to V_S near the surface at an early stage. The electronic band structure indicates that C_S , like V_S , exhibits p -type characteristics, which is in accordance with the observed p -type ARPES data for freshly exfoliated samples. Over time, all existing S vacancies are

consumed. Then, additional out-diffusing C atoms inevitably constitute the less stable C_{int} defects that exhibit n -type properties. This is consistent with the ARPES observations of changes from p -type to n -type with aging. We also confirmed that the stable charge states are neutral in the significant portion of the range of E_F for all the considered defects (Supplementary Fig. 10).

A question remains whether the carbon can be the origin of the n -type conductivity even in MoS₂ FETs where monolayer and/or CVD-grown samples are used, and thus C diffusion from bulk is excluded. In these cases, we speculate that C impurities may be incorporated during or after synthesis in the process of transfer for the measurement or device fabrication.

In summary, we have shown that C atoms near the surface of MoS₂ are responsible for the predominant n -type doping of natural minerals and the frequently observed nanometer-scale defects at the surface in STM images. Newly exfoliated MoS₂ surfaces occasionally exhibit p -type behavior when C atoms are barely detected. The p -type MoS₂ is due to S vacancies at the surface. The carbon-free p -type MoS₂ changes to n -type over time with the simultaneous increase in the amounts of C. The carbon atoms are supposed to migrate from the bulk to the near-surface region, resulting in unintentional n -type doping of the MoS₂ surface. The origin of the intrinsic p - and n -type doping of natural MoS₂ disclosed in this study provides new prospects to control doping for electronic and optoelectronic applications.

METHODS

Photoemission spectroscopy

Experiments were conducted using commercially available single-crystal 2H-MoS₂ flakes, referred to as “pristine MoS₂.” The pristine MoS₂ crystals were exfoliated using the scotch-tape method in ultra-high vacuum (UHV) with pressures ranging from 10⁻⁸ to 10⁻¹⁰ Torr. After transferring the exfoliated sample to the analysis chamber, the PES data were measured at the 10D beamline of the Pohang Accelerator Laboratory (PAL), which is equipped with Scienta DA30, R4000, and PHOIBOS 150 analyzers. For the exfoliated surface, the valence band and the C 1s and O 1s core levels were measured. A photon energy of 56 eV was used for the valence band and WF measurements, and 360 and 650 eV for C 1s and O 1s peaks, respectively. The binding energies were calibrated by measuring the Au Fermi energy or Au 4f_{7/2} core-level peak depending on the photon energy. A bias voltage of -10 V with an uncertainty of ±0.01 V was applied to the samples for the WF measurements. All the photoemission data were collected at RT. A homemade C evaporator, where an electron beam hits a carbon rod (99.99%), was used for carbon deposition in the PES experiments.

Scanning tunneling microscopy

STM experiments were carried out in an independent UHV chamber with a base pressure <3.0 × 10⁻¹⁰ Torr. For the experiments, single-crystal flakes of natural MoS₂ minerals mounted on pieces of a Si wafer were exfoliated using scotch tape in the UHV for in-situ measurements. The STM measurements were performed at RT using two STM instruments: a home-built STM and a commercial STM (SPICS Inc.). All STM images were taken in the constant current mode. The same e-beam C evaporator as in the PES experiments was used for carbon deposition in the STM experiments.

Density-functional theory calculations

Theoretical calculations were performed within the Vienna Ab-initio Simulation Package (VASP)⁵². The projector-augmented-wave pseudopotentials were used for the plane wave basis set for modeling the ion cores. The Perdew–Burke–Ernzerhof generalized gradient approximation was used for the exchange–correlation functional with the inclusion of spin polarization. The optB88-vdW van der Waals density-functional was used to describe the dispersion interactions in each system. A kinetic energy cutoff of 500 eV for the basis set and a 5 × 5 × 1 k-point mesh for the Brillouin zone integration were used for the 4 × 4 MoS₂ bilayer supercell. All atomic structures were fully relaxed until the forces on each atom were less than 0.01 eV/Å.

DATA AVAILABILITY

The data of this study are available from the corresponding author upon reasonable request.

Received: 13 March 2023; Accepted: 28 August 2023;

Published online: 05 September 2023

REFERENCES

- Wang, Q. H., Kalantar-Zadeh, K., Kis, A., Coleman, J. N. & Strano, M. S. Electronics and optoelectronics of two-dimensional transition metal dichalcogenides. *Nat. Nanotechnol.* **7**, 699–712 (2012).
- Schmidt, H., Giustiniano, F. & Eda, G. Electronic transport properties of transition metal dichalcogenide field-effect devices: surface and interface effects. *Chem. Soc. Rev.* **44**, 7715–7736 (2015).
- Manzeli, S., Ovchinnikov, D., Pasquier, D., Yazyev, O. V. & Kis, A. 2D transition metal dichalcogenides. *Nat. Rev. Mater.* **2**, 17033 (2017).
- Radisavljevic, B., Radenovic, A., Brivio, J., Giacometti, V. & Kis, A. Single-layer MoS₂ transistors. *Nat. Nanotechnol.* **6**, 147–150 (2011).
- Kim, S. et al. High-mobility and low-power thin-film transistors based on multi-layer MoS₂ crystals. *Nat. Commun.* **3**, 1011 (2012).
- Schmidt, H. et al. Transport properties of monolayer MoS₂ grown by chemical vapor deposition. *Nano Lett.* **14**, 1909–1913 (2014).
- Yin, Z. et al. Single-layer MoS₂ phototransistors. *ACS Nano* **6**, 74–80 (2012).
- Mak, K. F. et al. Tightly bound trions in monolayer MoS₂. *Nat. Mater.* **12**, 207–211 (2013).
- Bernardi, M., Palummo, M. & Grossman, J. C. Extraordinary sunlight absorption and one nanometer thick photovoltaics using two-dimensional monolayer materials. *Nano Lett.* **13**, 36643670 (2013).
- Wi, S. et al. Enhancement of photovoltaic response in multilayer MoS₂ induced by plasma doping. *ACS Nano* **8**, 5270–5281 (2014).
- Zong, X. et al. Photocatalytic H₂ evolution on MoS₂/CdS catalysts under visible light irradiation. *J. Phys. Chem. C* **114**, 1963–1968 (2010).
- Lukowski, M. A. et al. Enhanced hydrogen evolution catalysis from chemically exfoliated metallic MoS₂ nanosheets. *J. Am. Chem. Soc.* **135**, 10274–10277 (2013).
- Li, H. et al. Fabrication of single- and multilayer MoS₂ film-based FET for sensing NO at RT. *Small* **8**, 63–67 (2012).
- Bhimanapati, G. R. et al. Recent advances in two-dimensional materials beyond graphene. *ACS Nano* **9**, 11509–11539 (2015).
- Wang, F. et al. Progress on electronic and optoelectronic devices of 2D layered semiconducting materials. *Small* **13**, 1604298 (2017).
- Li, S. et al. p/n-Type modulation of 2D transition metal dichalcogenides for electronic and optoelectronic devices. *Nano Res.* **15**, 123–144 (2022).
- Lee, G. H. et al. Highly stable, dual-gated MoS₂ transistors encapsulated by hexagonal boron nitride with gate-controllable contact, resistance, and threshold voltage. *ACS Nano* **9**, 7019–7026 (2015).
- Zou, X. et al. Dielectric engineering of a boron nitride/hafnium oxide heterostructure for high-performance 2D field effect transistors. *Adv. Mater.* **28**, 2062–2069 (2016).
- Liu, Y. et al. Approaching the Schottky-Mott limit in van der Waals metal-semiconductor junctions. *Nature* **557**, 696–700 (2018).
- Lee, Y. H. et al. Synthesis of large-area MoS₂ atomic layers with chemical vapor deposition. *Adv. Mater.* **24**, 2320–2325 (2012).
- Liu, K. K. et al. Growth of large-area and highly crystalline MoS₂ thin layers on insulating substrates. *Nano Lett.* **12**, 1538–1544 (2012).
- Baugher, B. W. H., Churchill, H. O. H., Yang, Y. & Jarillo-Herrero, P. Intrinsic electronic transport properties of high-quality monolayer and bilayer MoS₂. *Nano Lett.* **13**, 4212–4216 (2013).
- Ahn, J. H., Parkin, W. M., Naylor, C. H., Johnson, A. T. C. & Drndić, M. Ambient effects on electrical characteristics of CVD-grown monolayer MoS₂ field-effect transistors. *Sci. Rep.* **7**, 4075 (2017).
- Zhang, Y., Ye, J., Matsuhashi, Y. & Iwasa, Y. Ambipolar MoS₂ thin flake transistors. *Nano Lett.* **12**, 1136–1140 (2012).
- Bao, W., Cai, X., Kim, D., Sridhara, K. & Fuhrer, M. S. High mobility ambipolar MoS₂ field-effect transistors: substrate and dielectric effects. *Appl. Phys. Lett.* **102**, 042104 (2013).
- Han, S. W. et al. Band-gap expansion in the surface-localized electronic structure of MoS₂(0002). *Phys. Rev. B* **86**, 115105 (2012).
- Jin, W. et al. Osgood, Direct measurement of the thickness-dependent electronic band structure of MoS₂ using angle-resolved photoemission spectroscopy. *Phys. Rev. Lett.* **111**, 106801 (2013).
- Alidoust, N. et al. Observation of monolayer valence band spin-orbit effect and induced quantum well states in MoX₂. *Nat. Commun.* **5**, 4673 (2014).
- Miwa, J. A. et al. Electronic structure of epitaxial single-layer MoS₂. *Phys. Rev. Lett.* **114**, 046802 (2015).
- Latzke, D. K. et al. Electronic structure, spin-orbit coupling, and interlayer interaction in bulk MoS₂ and WS₂. *Phys. Rev. B* **91**, 235202 (2015).
- Qiu, H. et al. Hopping transport through defect-induced localized states in molybdenum disulphide. *Nat. Commun.* **4**, 2642 (2013).
- McDonnell, S., Addou, R., Buie, C., Wallace, R. M. & Hinkle, C. L. Defect-dominated doping and contact resistance in MoS₂. *ACS Nano* **8**, 2880–2888 (2014).
- Lu, C. P., Li, G., Mao, J., Wang, L. M. & Andrei, E. Y. Bandgap, mid-gap states, and gating effects in MoS₂. *Nano Lett.* **14**, 4628–4633 (2014).
- Park, J. H. et al. Defect passivation of transition metal dichalcogenides via a charge transfer van der Waals interface. *Sci. Adv.* **3**, e1701661 (2017).
- Noh, J. Y., Kim, H. & Kim, Y. S. Stability and electronic structures of native defects in single-layer MoS₂. *Phys. Rev. B* **89**, 205417 (2014).
- Komsa, H. P. & Krasheninnikov, A. V. Native defects in bulk and monolayer MoS₂ from first principles. *Phys. Rev. B* **91**, 125304 (2015).
- Pandey, M. et al. Defect-tolerant monolayer transition metal dichalcogenides. *Nano Lett.* **16**, 2234–2239 (2016).

38. Singh, A. & Singh, A. K. Origin of n-type conductivity of monolayer MoS₂. *Phys. Rev. B* **99**, 121201 (2019). (R).
39. Addou, R., Colombo, L. & Wallace, R. M. Surface defects on natural MoS₂. *ACS Appl. Mater. Interfaces* **7**, 11921–11929 (2015).
40. Bampoulis, P. et al. Defect dominated charge transport and Fermi level pinning in MoS₂/metal contacts. *ACS Appl. Mater. Interfaces* **9**, 19278–19286 (2017).
41. Liu, X., Balla, I., Bergeron, H. & Hersam, M. C. Point defects and grain boundaries in rotationally commensurate MoS₂ on epitaxial graphene. *J. Phys. Chem. C* **120**, 20798–20805 (2016).
42. Böker, T. et al. Band structure of MoS₂, MoSe₂, and a-MoTe₂: angle-resolved photoelectron spectroscopy and ab initio calculations. *Phys. Rev. B* **64**, 235305 (2001).
43. Vancsó, P. et al. The intrinsic defect structure of exfoliated MoS₂ single layers revealed by scanning tunneling microscopy. *Sci. Rep.* **6**, 29726 (2016).
44. Donarelli, M., Bisti, F., Perrozzi, F. & Ottaviano, L. Tunable sulfur desorption in exfoliated MoS₂ by means of thermal annealing in ultra-high vacuum. *Chem. Phys. Lett.* **588**, 198–202 (2013).
45. Zhang, X. et al. Unravelling the effect of sulfur vacancies on the electronic structure of the MoS₂ crystal. *Phys. Chem. Chem. Phys.* **22**, 21776–21783 (2020).
46. Chen, Y. et al. Tuning electronic structure of single layer MoS₂ through defect and interface engineering. *ACS Nano* **12**, 2569 (2018).
47. Bussolotti, F., Yang, J., Kawai, H., Wong, C. P. Y. & Goh, K. E. J. Impact of S-vacancies on the charge injection barrier at the electrical contact with the MoS₂ monolayer. *ACS Nano* **15**, 2686–2579 (2021).
48. Siao, M. D. et al. Two-dimensional electronic transport and surface electron accumulation in MoS₂. *Nat. Commun.* **9**, 1442 (2018).
49. McGovern, I. T., Williams, R. H. & Mee, C. H. B. Electronic properties of cleaved molybdenum disulphide surfaces. *Surf. Sci.* **46**, 427–440 (1974).
50. Zhang, F. et al. Carbon doping of WS₂ monolayers: bandgap reduction and p-type doping transport. *Sci. Adv.* **5**, eaav5003 (2019).
51. Cochran, K. et al. Intentional carbon doping reveals CH as an abundant charged impurity in nominally undoped synthetic WS₂ and WSe₂. *2D Mater.* **7**, 031003 (2020).
52. Kresse, G. & Furthmüller, J. Efficient iterative schemes for ab initio total-energy calculations using a plane-wave basis set. *Phys. Rev. B* **54**, 11169 (1996).

ACKNOWLEDGEMENTS

This research was supported by the Basic Science Research Program (2021R1A2C1006113, 2020R1A2B5B02001876, 2021R1A2C1006039 and 2020R1A2C2013757), Nano-Material Technology Development Program (2021M3H4A1A02055667), and the Creative Materials Discovery Program (2020M3D1A1110548) through the National Research Foundation of Korea (NRF) funded by Ministry of Science and ICT. This work was supported by the National Supercomputing Center with supercomputing resources, including technical support (No. KSC-2021-CRE-0258, KSC-2021-CRE-0567, KSC-2021-CRE-0574, KSC-2022-CRE-

0497). The experiments at PLS were supported in part by the Ministry of Science and ICT and POSTECH.

AUTHOR CONTRIBUTIONS

Y.P., D.J., L.T.S., J.B., E.L., D.O., Y.D.K., C.C.H. performed the ARPES experiments. J.W., S.P., and G.L. performed the STM experiments. N.L., J.Y.L., H.K., and G.S.L. performed the DFT calculations. C.C.H., G.S.L., and G.L. supervised the project.

COMPETING INTERESTS

The authors declare no competing interests.

ADDITIONAL INFORMATION

Supplementary information The online version contains supplementary material available at <https://doi.org/10.1038/s41699-023-00424-x>.

Correspondence and requests for materials should be addressed to Youngsin Park, Geunseop Lee, Geunsik Lee or Chan-Cuk Hwang.

Reprints and permission information is available at <http://www.nature.com/reprints>

Publisher's note Springer Nature remains neutral with regard to jurisdictional claims in published maps and institutional affiliations.



Open Access This article is licensed under a Creative Commons Attribution 4.0 International License, which permits use, sharing, adaptation, distribution and reproduction in any medium or format, as long as you give appropriate credit to the original author(s) and the source, provide a link to the Creative Commons license, and indicate if changes were made. The images or other third party material in this article are included in the article's Creative Commons license, unless indicated otherwise in a credit line to the material. If material is not included in the article's Creative Commons license and your intended use is not permitted by statutory regulation or exceeds the permitted use, you will need to obtain permission directly from the copyright holder. To view a copy of this license, visit <http://creativecommons.org/licenses/by/4.0/>.

© The Author(s) 2023